

Graphene on mica probed by scanning tunneling microscopy: networks of ABA and ABC stacked graphene and corrugation of the monolayer

Silke Hattendorf,* Alexander Georgi, Viktor Geringer, Marcus Liebmann, and Markus Morgenstern

*II. Physikalisches Institut B,
RWTH Aachen and JARA-FIT,
Otto-Blumenthal-Straße, 52074 Aachen*

(Dated: July 24, 2012)

Graphene flakes are prepared on freshly cleaved mica by exfoliation in different environments and studied by scanning tunneling microscopy in ultra high vacuum down to the atomic length scale. On the monolayer, we observed an overall roughness of about 60 pm, after heating the sample to 180° C which is larger than on similarly prepared multilayers (24 pm) and larger than on monolayers which have been mapped recently by atomic force microscopy without heating (24 pm). A slight preference for a distinct wave length ($\lambda \simeq 8$ nm) of corrugations could be determined using an autocorrelation analysis. On few-layer graphene, a triangular network of partial dislocations separating ABC stacked and ABA stacked graphene was found similar to the networks occasionally visible on freshly cleaved HOPG. We found differences in the electronic structure of ABC and ABA stacked areas by scanning tunneling spectroscopy, i.e., a pronounced peak at 0.25 eV above the Fermi level exclusively in the ABA areas, which is largely responsible for the different apparent heights.

PACS numbers: 61.72.Nn, 73.22.Pr, 61.48.Gh

I. INTRODUCTION

Since Geim and Novoselov succeeded in producing monolayer graphene flakes by exfoliation¹, graphene developed into a favourite research topic due to its two-dimensional nature and its unique combination of electronic, mechanical and optical properties accompanied by chemical inertness.^{2,3}

Recently, trilayer graphene, which exhibits two different possibilities of stacking, came into focus⁴⁻⁷, since it was predicted that an electric field \underline{E} can open a band gap of up to 200 meV for ABC (rhombohedral) stacking, but not for the conventional ABA (Bernal) stacking.⁸⁻¹⁶ Interestingly, it has been shown, in addition, that thicker layers of ABC stacking exhibit conducting surface states in the absence of \underline{E} , but an insulating bulk, very similar to weak topological insulators.¹⁶ In addition, high-temperature superconductivity driven by the large density of states at the surface has been proposed for thicker ABC stacked layers.¹⁷ The two different stackings of trilayers could be distinguished experimentally by gate dependent infrared spectroscopy,^{7,18} by Raman spectroscopy,^{19,20} and by differences in the temperature- or magnetic-field dependent transport properties.^{5,6,21,22} This revealed, e.g., that about 15 % of the sample area prepared by exfoliation is ABC stacked,¹⁹ and that the predicted distinction in band-gap opening exists, although so far only with a band gap below 10 meV.^{5,20,23} These methods, however, are limited in lateral resolution to about 1 μm , thus, they are not able to resolve finer stacking orders in graphene. Based on earlier work using HOPG,²⁴⁻²⁸ we will firstly show that scanning tunneling spectroscopy (STS) can distinguish ABA and ABC areas exploiting a peak in scanning tunneling spectroscopy found only on the ABA stacking areas. We identified a

region on multilayer graphene on muscovite mica which exhibits a triangular network of dislocation lines separating ABC and ABA areas with sizes down to (200 nm)². For such a network, one can anticipate, based on the theoretical predictions, that a vertical electric field would result in a triangular network of graphene quantum dots with tunable barriers.

Secondly, we investigated the corrugation of graphene on mica prepared with a heating step to 180-190° C. The rms value of the surface roughness was about 60 pm for monolayer and 25 pm for multilayer and a slight preference for a wavelength of 8 nm in the corrugation pattern was found. The roughness of the monolayer was larger than the 24 pm determined previously by atomic force microscopy (AFM) without heating the sample prior to the measurement.²⁹ Water intercalation between graphene and mica, leading, in addition, to a p-type doping of graphene,³⁰ has been regularly found by AFM after preparation in air or even at strongly reduced humidity.^{30,31} We tried to reduce the density of water below the graphene by exfoliating the graphene in Ar atmosphere with less than 2 ppm of water, however, without success. The water below the graphene remains to cover about 50 % of the area below graphene which implies that the water is not trapped during the exfoliation.

II. EXPERIMENT

Graphene samples were prepared by mechanical exfoliation¹ on freshly cleaved muscovite mica (highest quality "V1", Plano GmbH, Wetzlar, Germany), an aluminosilicate with the formula unit $\text{KAl}_2(\text{Si}_3\text{Al})\text{O}_{10}(\text{OH})_2$ ³² and a layered structure consist-

ing of one layer of octahedrally coordinated Al^{3+} ions surrounded by two layers of tetrahedral Si^{4+} ions. Every fourth Si^{4+} ion is replaced by an Al^{3+} , resulting in an excess negative charge, which is compensated by K^+ ions connecting the triple layers. Mica can be cleaved along the K^+ layers with large areas (several $100 \mu\text{m}^2$) of mono-atomic flatness. However, the density distribution of K^+ on the two cleaved surfaces is not perfectly homogeneous leading to hydrophilic properties which trigger the formation of potassium carbonate islands on the surface, if ambient water is present.^{33,34}

In order to reduce the influence of water, we cleaved mica and deposited graphene on top by exfoliation not only under ambient conditions, but also within a dry air box with reduced though not explicitly controlled water density as well as within an Ar box with a measured H_2O concentration below 2 ppm.

Thin graphene flakes were identified afterwards using optical polarization microscopy under ambient conditions as described by Dorn et. al.³⁵ The number of layers was determined by Raman spectroscopy at laser excitation wavelength of 532 nm .³⁶ To avoid extensive heating of the sample, the laser power was kept below 2 mW and the measurement time was $5\text{-}10 \text{ s}$. To determine the number of layers in the case of few-layer flakes as presented in section III B, AFM was used to measure the height difference between a monolayer area of graphene and the multilayer area of interest.

To avoid possible chemical residues on the graphene surface resulting from lithography,³⁷ indium micro-soldering was used for contacts as initially described by Girit et. al.³⁸ This required heating of the sample to $180\text{-}190^\circ\text{C}$ in order to melt the In onto the graphene surface properly, which might have influences on the observed corrugation as discussed in section III C.³⁹

The STM measurements were carried out at 300 K in a home-built UHV system operating at a background pressure of $1\text{-}2 \cdot 10^{-8} \text{ Pa}$. Tungsten tips were prepared by electrochemical etching and subsequently short heating inside the ultrahigh vacuum chamber to remove the tungsten trioxide layer formed during the etching process.⁴⁰ The positioning of these tips above the graphene flakes is achieved using a long-range optical microscope with resolution down to $10 \mu\text{m}$. A bias voltage V of $V = 0.2\text{-}0.6 \text{ V}$ or $V = -0.2\text{-}-0.5 \text{ V}$ was applied to the graphene sample and currents of $I = 0.05\text{-}0.5 \text{ nA}$ were used for constant-current images. The dI/dV -curves were acquired by applying an additional ac-voltage with a frequency of 1.4318 kHz and a modulation amplitude of $V_{\text{mod}} = 30 \text{ mV}$ and detecting the resulting in-phase ac current by a lock-in amplifier.

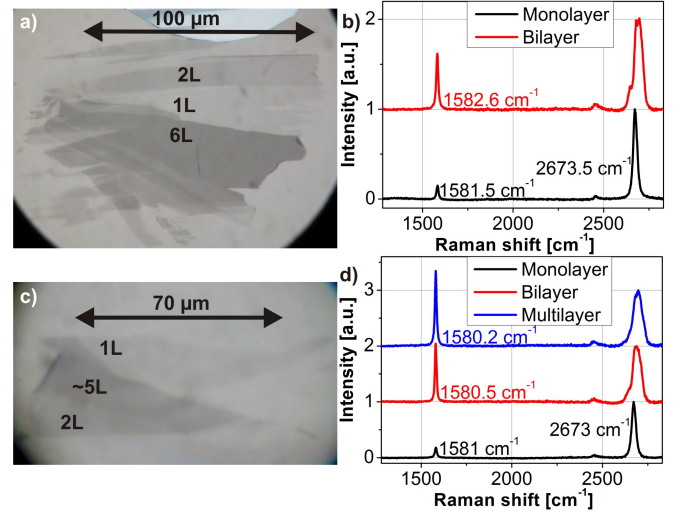


FIG. 1. (a)+(c) Optical images of samples prepared by exfoliation in the dry box recorded with polarization microscopy; layer thickness n in monolayers of graphene is marked as $n\text{L}$. (b)+(d) Corresponding Raman spectra of the regions marked in the optical images as 1L (Monolayer), 2L (Bilayer) and 5L (Multilayer).

III. RESULTS AND DISCUSSION

A. Raman spectroscopy and atomic force microscopy

Figure 1 shows optical images of some of the prepared samples along with the corresponding Raman spectra. The number of layers is identified as usual by analyzing the shape and position of the 2D peak as described, e.g., by Malard et. al.³⁶ For thicker layers the steps between monolayer and adjacent layers are imaged by tapping mode AFM in order to determine the height as given in Fig. 1. Fig. 2 shows a tapping-mode AFM image of the sample prepared in the argon box at relative humidity below 2 ppm. The monolayer is folded back at the edge and several first-layer and second-layer water adlayers as well as larger bubbles are visible, which are believed to be trapped between the graphene layer and the mica substrate.^{30,31,41} The area covered by water underneath the flake is roughly 53%, i.e. even larger than the area obtained after preparation under ambient conditions (22%). Like Shim et. al.³⁰, we were unable to see any relationship between relative humidity and water coverage during exfoliation. As water coverage can be even larger than a single layer,^{30,31} the AFM images do not exclude the possibility of more than one water adlayer below the graphene directly. However, the distinct topography between the lower and the upper areas of graphene disfavor such an assumption. A similar distinct topography, in particular, a distinct apparent height of adjacent steps, is visible in STM measurements (s. Fig. 3). Thus, most likely, a submonolayer of water is trapped between the graphene and the mica even after preparation in nearly

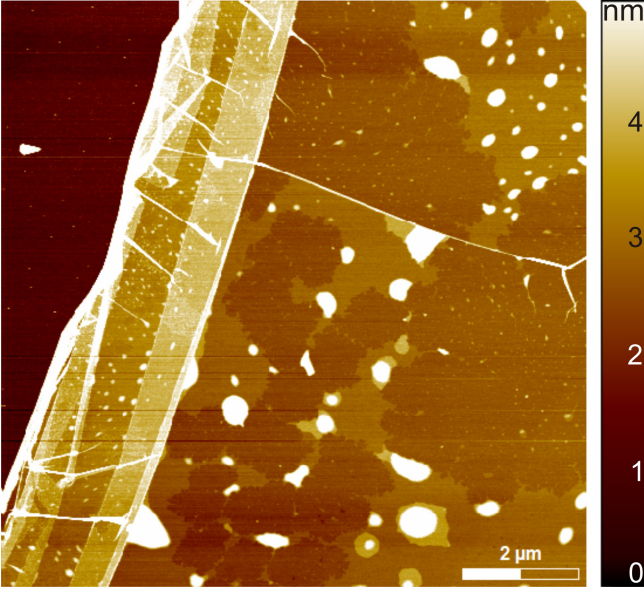


FIG. 2. Tapping mode AFM image acquired under ambient conditions of a graphene monolayer on mica with folded edge on the left; cantilever stiffness: $\sim 40 \frac{\text{N}}{\text{m}}$, frequency: 300.25 kHz, set-point: 52%, free amplitude: 31 nm; the sample was prepared in an argon box; water underneath the monolayer (elevated areas) covers about 53% of the area below the graphene.

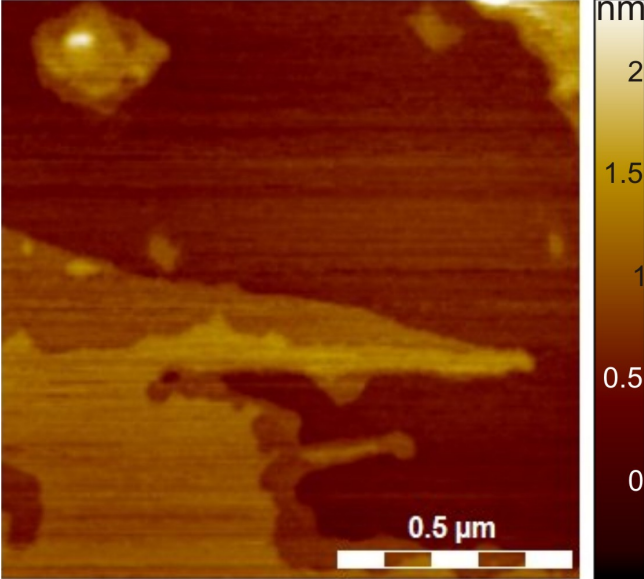


FIG. 3. STM image showing water underneath a monolayer graphene (s. Fig. 1(a)) prepared by exfoliation in the dry box. $V = -0.5 \text{ V}$ $I = 0.2 \text{ nA}$.

H_2O free environment. This is surprising since the water adlayer on uncovered mica has been shown to disappear below a relative humidity of 20 %.⁴² We do not know the origin of this water. Possibilities could be that the water diffuses below the graphene after preparation, when exposed to ambient conditions again or it diffuses out of the

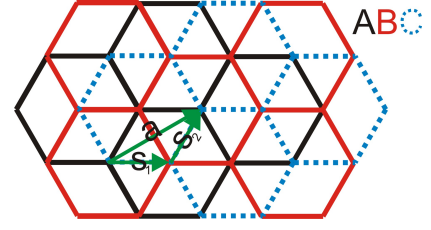


FIG. 4. Sketch of ABC stacked trilayer graphene with the three layers colored differently as marked. Only the carbon-carbon bonds are shown as lines. The arrow labeled 'a' marks a Burgers vector of a possible dislocation in the upper graphene layer separating two areas of the same stacking. This dislocation can be separated into two shorter (and thus energetically more favorable) partial dislocations (labeled 's₁' and 's₂'). Since 's₁', for example, transforms an A-layer into a C-layer, adjacent stacking-types of ABC and CBC result, i.e. an area of different stacking.

mica, e.g., due to the pressure applied during exfoliation.

B. Stacking-faults in few-layer graphene on mica

For more than two layers, the stacking order of graphene has to be taken into account. There are several ways of stacking. The most stable one is called Bernal-stacking showing an ABA sequence as illustrated in Fig. 4. Another obvious possibility is rhombohedral stacking with ABC sequence being energetically slightly less favorable by about 0.18 meV per atom.¹² For both stackings, the distances between carbon atoms within the graphene sheet (1.418 Å) and the separations of graphene layers (3.348 Å) are identical.⁴³

The lateral energy barrier between these two stackings has been calculated to be about 2 meV per atom only, which favors a network of stacking faults.¹² Therefore, partial dislocations with a Burgers vector $s_1 = \frac{1}{3}a <1\bar{1}00>$ are required to transform ABA graphite into ABC graphite and back again (s. Fig. 4). A network of partial dislocations connecting triangular ABA and ABC areas has indeed been observed in highly oriented pyrolytic graphite (HOPG) by electron microscopy.^{44–47} The partial dislocation character has been proven directly in dark-field images.⁴⁴ STM images of such dislocation networks were recorded subsequently revealing an apparent height contrast between differently stacked areas.^{24–28} Kobayashi et. al.²⁸ showed, in addition, that this contrast changed in intensity across a buried step edge, which was qualitatively explained by a difference in the local density of states (LDOS) resulting from an interference of electronic waves normal to the surface. STM images of the few-layer graphene area shown optically in Fig. 1 (a) are displayed in Fig. 5 revealing an area with a triangular pattern. Triangles pointing in different directions exhibit apparent heights differing by 1–4 Å. Due to the similarity of these patterns to the patterns found previously on HOPG,^{24–28,44–47} we assign it to a

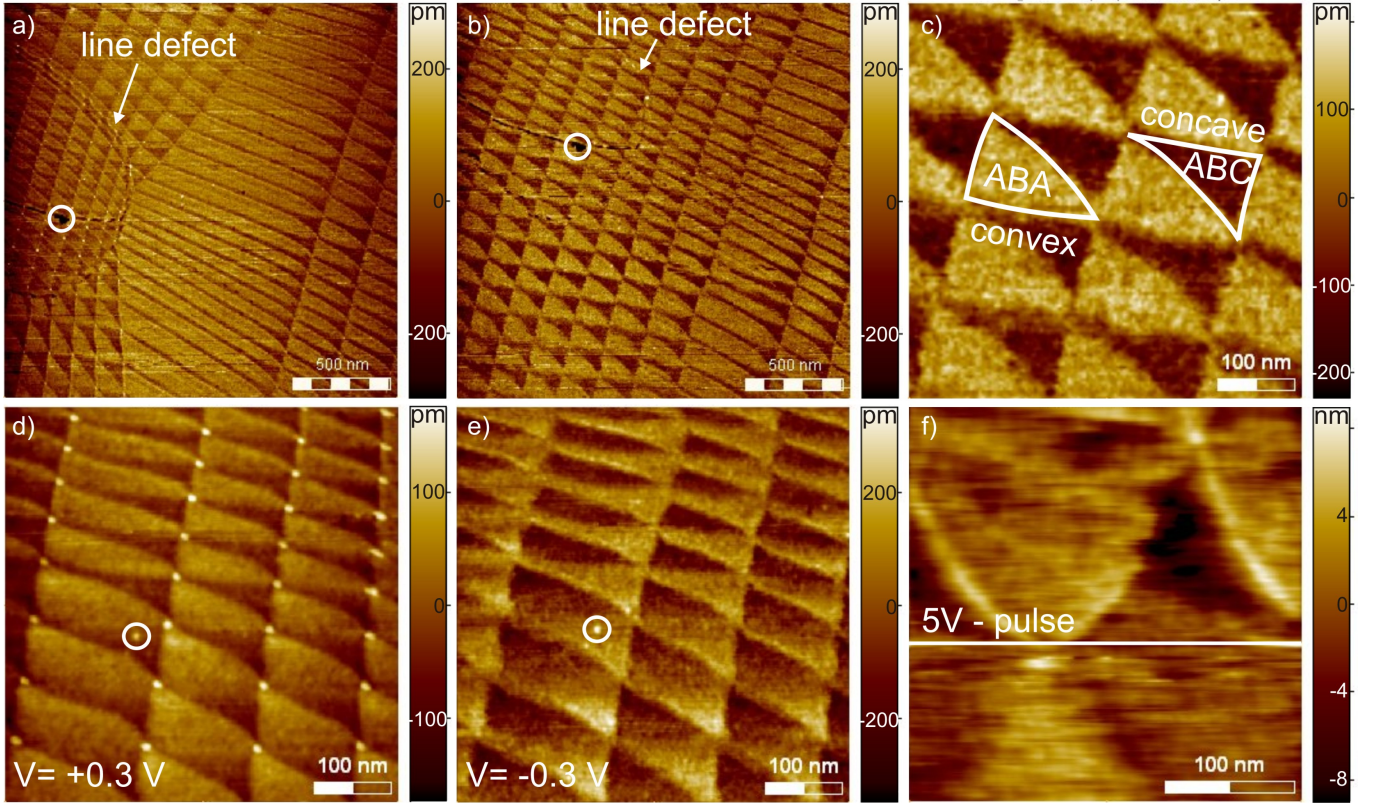


FIG. 5. STM images of dislocation network on few-layer (6 ± 1 layers) area of graphene on mica. (a), (b) are recorded on the same area with 2 hours in between; $V = 0.4$ V, $I = 0.1$ nA, scan speed: $2 \frac{\mu\text{m}}{\text{s}}$; white circles highlight a defect which marks the same area in (a) and (b); a line defect is indicated in both images; notice the change of the network towards a more regular structure from (a) to (b); (c) Zoom into the lower left edge of (b); white lines mark dislocation lines, which according to the indicated curvature presumably encircle ABA and ABC areas as marked; (d), (e) are recorded subsequently on the same area with different voltage polarity; white circles mark a defect, i.e. the same position in both images; (d) $V = 0.3$ V; $I = 0.15$ nA; $1 \frac{\mu\text{m}}{\text{s}}$; (e) $V = -0.3$ V; $I = 0.15$ nA; $1 \frac{\mu\text{m}}{\text{s}}$; notice the contrast inversion between (d) and (e). (f) STM image recorded at $V = 0.4$ V; $I = 0.2$ nA; $0.6 \frac{\mu\text{m}}{\text{s}}$; during scanning, a 5 V pulse is applied at the white line as marked, leading to contrast inversion.

dislocation network separating triangular areas of ABA and ABC stacked graphene. Fig. 5 (a) and (b) show two large-scale images, which have been measured subsequently on the same area of the sample. Obvious changes in the pattern towards a more regular network emphasize the mobile nature of the dislocation network, which is a well-known property of partial dislocations.⁴⁸ Within the first image, some dislocation lines appear to be pinned to the defect line marked in Fig. 5 (a), but are depinned two hours later in Fig. 5 (b). We checked carefully that the appearance of such a relaxed structure does not depend on scan direction, which, however, does not exclude that the depinning was initiated by the scanning process. The large scale mobility of the network underlines that the apparent height is not caused by a topographic feature, which is unlikely to be moved strongly at 300 K once and then remain stable. The triangular shape of the pattern is, in addition, in line with the three possible directions of Burgers vectors transforming ABA into ABC areas. In Fig. 5 (c), the shape of a dark and a bright region is marked by white lines. One observes that the bright

one is a triangle with convex edges, while the dark one exhibits concave edges. Based on this shape, the stacking order of the different areas can be assigned. Since ABC graphite is energetically less favorable,¹² there is a force on the dislocation lines in the direction of ABC stacking, resulting in concave shapes for these areas. In turn, this identifies the darker areas observed at positive sample bias as ABC regions or, more generally, as the stacking fault regions. The crossing points of the dislocation lines, called nodes, require an energetically costly local AA stacking or a vacancy due to symmetry. These nodes often appear brighter than the surrounding area (e.g Fig. 5 (d)).

The contrast between ABA and ABC stacked areas as shown in Fig. 5(d) and (e), can invert with bias polarity. This was not observed on HOPG, where only a gradual change was found.²⁴ Moreover, the contrast could even be inverted by voltage pulses changing the shape of the tip. This is shown in Fig. 5(f) and verified by imaging the complete area prior and after the voltage pulse with the same tunneling voltage of 0.4 V (not shown). Since the

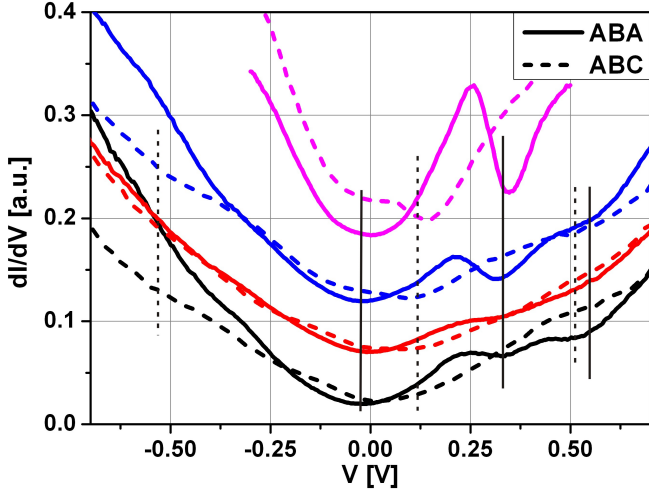


FIG. 6. dI/dV -spectra acquired on ABA-stacked (solid) and ABC-stacked (dashed) regions. Spectra of the same color were acquired on adjacent regions directly after each other. The black, red and blue measurements are stabilized at $V = 1$ V and $I = 0.2$ nA, the pink ones at $V = 0.5$ V and $I = 0.2$ nA, $V_{\text{mod}} = 30$ meV. Measurements are shifted vertically for clarity. Vertical lines mark minima. Notice that the pink spectra are slightly shifted upwards with respect to the other ones.

tip where we occasionally observed the contrast change by pulsing was rather unstable as visible in the STM image and exhibited an unusually large decay length in $I(z)$ curves, we believe that the tip chemistry and, thus, the surface potential of the tip changed significantly during the pulse. Importantly, all these observations strongly suggest that the observed contrast is not of topographic origin but of an electronic one.

To further analyze the electronic differences, dI/dV -spectra, which are proportional to the local density of states (LDOS), were acquired on ABC and ABA areas as shown in Fig. 6. The spectra exhibit several minima marked by vertical lines and an obvious peak at $V = 0.25$ V only on the ABA areas. Also the positions of the minima are different for differently stacked areas as marked. Since the curves are acquired alternately on ABA- and ABC-stacked areas, one can exclude that these spectroscopic differences are caused by a tip change. The global minimum is found around 0 mV for ABA areas and at 125 mV for ABC areas. This might indicate a relative offset of the Dirac point energy E_D . The peaks and dips are slightly moved upwards by about 20 mV in the spectra acquired at smaller tip-surface distance (pink curves). This indicates an upwards band bending at the graphene surface induced by the work function mismatch between tip and graphene and implies an electric field penetration into the graphene sample.⁴⁹ No band gap is observed neither on the ABA nor on the ABC areas, which means that a band gap, if present, is smaller than about 100 meV being the energy resolution of the experiment.⁴⁹ Theoretical calculations^{10,11,16} of ABA and ABC stacked graphene find complex band structures changing with electric field,

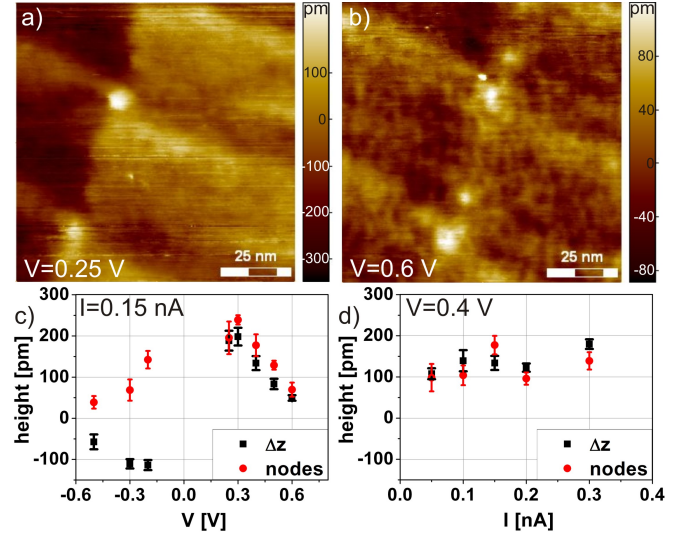


FIG. 7. (a) Small scale STM image of multilayer graphene with stacking faults, $V = 0.25$ V, $I = 0.15$ nA; (b) same area as in (a), $V = 0.6$ V; $I = 0.15$ nA. (c) Voltage dependency of the averaged height difference between ABA and ABC areas Δz and of the average height of the nodes with respect to the highest stacking area in the surrounding (nodes); $I = 0.15$ nA. (d) Current dependency of the same quantities as displayed in (c); $V = 0.4$ V.

which, however, are largely symmetric with respect to E_D . We checked that they cannot explain a single peak at +0.25 eV, which is only found in ABA areas, using reasonable assumptions for the electric field penetration depending on tip-sample distance and screening. Since the peak is observed close to the tentative E_D of the ABC area, i.e. where a gap exists in ABC stacked areas, it might indicate a confinement of electronic states within the ABA area (see below).

Based on the spectroscopic data, we can show more quantitatively that the apparent height difference Δz between ABA and ABC stacked areas is of electronic origin. Therefore, we first measure the dependency of Δz on sample voltage V and current I . Figure 7(a) and (b) show part of the dislocation network imaged at two different V , where the height difference between the darker areas (ABC) on the left and the brighter areas (ABA) on the right has been used to measure Δz . The results are displayed in Fig. 7(c) and (d). In addition, the height of the nodal points, is determined with respect to the surrounding area appearing the highest and is shown as 'nodes' in Fig. 7(c) and (d), too. Obviously, the current dependency of Δz is weak while the voltage dependency is pronounced. The contrast between ABA and ABC areas inverts with voltage polarity, increases with decreasing $|V|$, and is largest around $V = 0.25$ V. Similar trends are observed for the contrast of the nodes, except that the nodes always appear higher than the surrounding. Partly, the dislocation lines exhibit a distinct contrast as visible in Fig. 7(b), but we did not evaluate this contrast

in more detail, because it appears only at certain V .

Next, we calculate the apparent height difference expected from the dI/dV curves. According to Tersoff and Hamann⁵⁰, the tunneling current I at voltage V depends on the LDOS of the tip $\rho^t(E)$ and the LDOS of the sample at the position below the tip $\rho^s(E)$ according to:

$$I \propto \int_0^{eV} \rho^t(E_F + \epsilon) \cdot \rho^s(E_F - eV + \epsilon) \cdot T(\epsilon, V, z) d\epsilon. \quad (1)$$

Here, E_F is the Fermi level, z is the distance between the tip and the sample surface, and $T(\epsilon, V, z)$ is the transmission coefficient of the tunneling process being exponentially dependent on z . Since a constant I is used to stabilize the vertical tip position with respect to the sample, a difference in LDOS of the different sample areas results in a change of z and consequently appears as a height difference Δz in constant-current images, even if the sample is flat. To estimate the expected Δz at voltage V , the dI/dV curves are integrated between 0 V and the applied voltage V_{meas} and translated into a height difference using $I(z)$ -spectra. The procedure is illustrated in Fig. 8 exemplary for the pink curves of Fig. 6. As can be seen by comparing Fig. 8(a) and (b), the dI/dV values in the completely filled area of the curve are larger for ABA-stacked graphene than for ABC-stacked graphene. Thus, the resulting height difference must increase by reducing the voltage from V_{stab} to V_{meas} . This is indeed observed experimentally. To determine the expected Δz quantitatively, the filled area underneath the dI/dV -curves, ranging from $V = 0$ V to V_{meas} , is divided firstly by the hatched area, ranging from $V = 0$ V to V_{stab} . Then, the resulting ratios obtained for ABA and ABC area are divided by each other and are used to determine a height difference Δz from the exponential $I(z)$ curve as illustrated in Fig. 8(c). For the V_{meas} in the example, an additional height difference of 111 pm results, which has to be added to the height difference observed at V_{stab} to determine Δz . Notice that the exponential $I(z)$ curve guarantees an independence of the found Δz from the chosen z value in the $I(z)$ curve.

Figure 9 shows the result of such a calculation as a function of V_{meas} using dI/dV curves stabilized at $V_{\text{stab}} = 1$ V (red line) in comparison with the determined Δz from Fig. 7(c) (black squares). Dashed lines mark the error bar determined from five pairs of dI/dV curves recorded on different positions. As the topographic data at $V = 1$ V became rather noisy, the height difference at $V = 0.6$ V was added as the offset to determine the calculated heights. Note that the simulated height difference changes very little between $V = 0.6$ and $V = 1$ V. The characteristics of the measured $\Delta z(V)$ curve, i.e., the change of contrast around $V = 0$ V and the decrease of contrast with increasing $|V|$, are well reproduced by the calculation, although the experimental $|\Delta z|$ values are slightly larger. The reasonable agreement excludes a dominating influence of a mechanical interaction between the tip and the graphene as well as of the electric field of the tip onto the apparent height, since both

are changing with distance being significantly different in the constant-current image used to determine the experimental Δz and in the dI/dV curve used to determine the calculated Δz . Since the contrast inversion with voltage polarity excludes a dominating influence of topography, we conclude that the different LDOS is primarily responsible for the contrast between ABA and ABC areas in constant-current images.

The question remains: what causes the differences in LDOS, respectively the LDOS peaks? Intrinsic differences of the band structure could be excluded as discussed above. A Fabry-Perot type interference, similar to a proposal by Kobayashi et. al.²⁸, was considered. The idea is the following: electrons tunneling into the graphene multi-layer are reflected back at the interface between graphene and mica forming an interference pattern with the incoming electrons. Depending on the energy of the electrons, this interference can be constructive or destructive causing peaks and minima in the LDOS. The energy of these peaks is straightforwardly calculated using the energy dispersion of graphite orthogonal to the surface:

$$E = \frac{(\hbar k)^2}{2m_{\perp}} - 2\gamma_1 \quad (2)$$

with $m_{\perp} = \frac{\hbar^2}{2c^2\gamma_1}$, the interlayer distance $c = 335$ pm and the interlayer hopping parameter $\gamma_1 = 0.39$ eV as well as the condition for constructive interference:

$$k = \frac{2\pi}{\lambda} = \frac{\pi n}{cN} \quad (3)$$

with $n \in \mathbb{N}$ and N being the number of layers in the graphene sheet.

The stacking fault might scatter the electrons isotropically due to the band gap in its interior prohibiting the vertical interference, and, thus, explaining the absence of strong peaks in the ABC region. However, for the determined layer thickness $N = 6$, the four lowest energy peaks would be at about -0.7 eV, -0.35 eV, +0.2 eV, +0.9 eV with respect to E_D in clear disagreement with the measured spectra exhibiting a single strong peak at about 0.25 eV and maybe a smaller one at 0.4 eV. Layer numbers N between 5 and 7 have been checked, in accordance with the maximum uncertainty of the layer thickness determined by AFM, but without success. Thus, we do not have any quantitative model for the strong peak, albeit it could be that an additional lateral confinement by the gap within the interior of the ABC area strengthens the vertical Fabry-Perot resonance in the ABA region which is closest to E_D , i.e. the one at 0.2 eV.

C. Corrugations of graphene on mica

Finally, we consider the corrugation of graphene on mica. Even freely suspended graphene was found to be corrugated by about 100 pm using electron microscopy.⁵¹

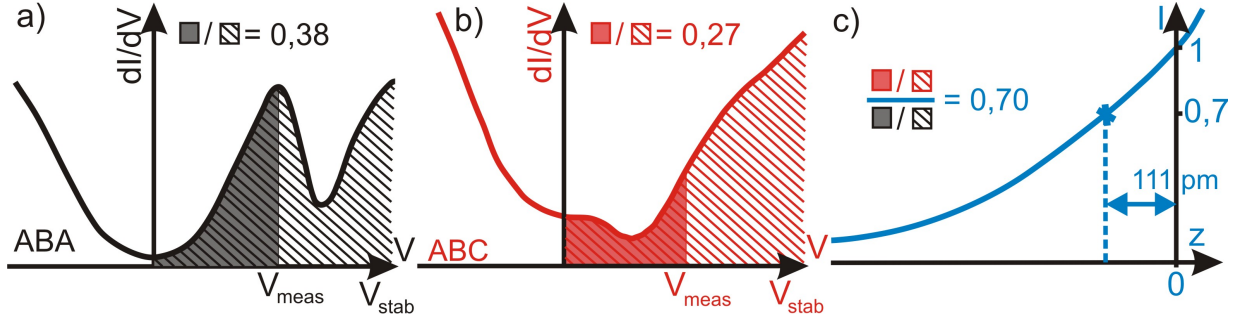


FIG. 8. Illustration how to determine the expected height difference between ABA- and ABC-stacked areas from dI/dV -spectra; (a),(b) dI/dV -spectra of ABA- and ABC-stacked areas as marked (same as pink curves in Fig. 6); the hatched area up to V_{stab} has to be integrated to determine the current relevant for the stabilization during the dI/dV curve, while the completely filled area up to V_{meas} determines the current at V_{meas} ; the ratio between filled and hatched areas is given above the curves; (c) sketch of the distance dependence of the current; the ratio of the ratios from (a) and (b), 0.7, is marked symbolically and at the I -axis; it is translated to a height difference by the $I(z)$ curve as marked.

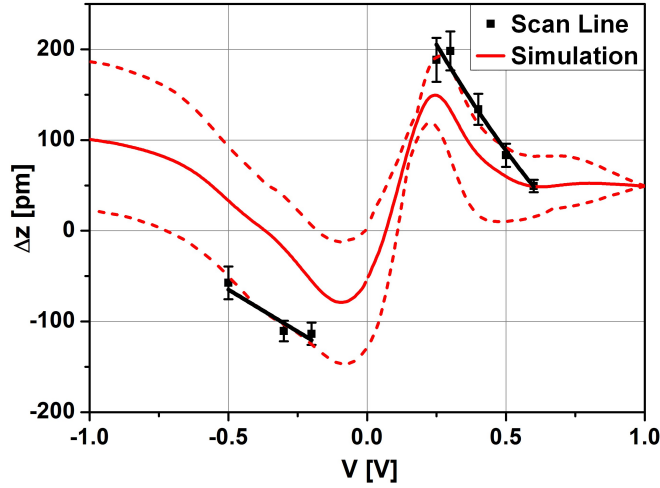


FIG. 9. Black Squares: height difference Δz between ABA- and ABC-stacked areas measured in constant-current images (same data as in Fig. 7(c)); black solid lines serve as guide-to-the-eye; red solid line: averaged height differences calculated from five dI/dV -spectra stabilized at $V_{\text{stab}} = 1$ V according to the method illustrated in Fig. 8; red dashed lines: error bars resulting from fluctuations for dI/dV -spectra taken at different positions on the sample.

This has firstly been explained by a coupling between in-plane and out-of-plane phonons,⁵² stabilizing graphene against thermal vibrations, that would normally crumble a two-dimensional material.⁵³ Later experiments showed a strong influence of the preparation conditions on rippling, in particular, of the heating process.⁵⁴ To analyze the influence of substrates, the graphene morphology has been measured, e.g., for graphene deposited on SiO_2 ,^{39,55–59} muscovite mica,^{29,31} hexagonal boron nitride,⁶⁰ and graphene grown on copper foils.^{61–63} Graphene on copper exhibited very large roughness due to the roughness of the underlying copper substrate and additional strain which builds up during cooling after

growth and gets released by the formation of ripples and wrinkles.^{62,63} Exfoliated graphene on silicon dioxide also exhibits a large roughness of $\sigma_{\text{rms}} = 140 - 320$ pm due to the underlying substrate and partly an intrinsic rippling observed, if the graphene is not in complete contact with the SiO_2 .^{39,57–59,64} In the latter case, the suspended areas could be hysteretically lifted by electrostatic forces.⁶⁴ Graphene on mica was studied firstly by AFM revealing a roughness of 24 pm for the monolayer, which, however, might be limited by the lateral resolution of the AFM given as 7 nm.²⁹ STM data of graphene on mica have also been published with an intentionally complete intercalated water layer between the mica and graphene making a roughness analysis difficult. Nevertheless, a preferential roughness value of 15 pm has been given.⁴¹ The smallest graphene roughness was observed so far on the flat van-der-Waals surface of hexagonal boron nitride(0001) being between 2 and 17 pm, which interestingly, led to reduced potential fluctuations, too.^{60,65}

Fig. 10 (a) and (b) show typical STM images of monolayer and few-layer graphene on mica recorded in areas neither exhibiting signs of underlying water nor of a stacking fault. A line fit and a low-pass filter in the Fourier transformation with a cut-off wavelength of 3 nm and a first-order butterworth profile were applied to remove the influence of occasional changes in the tip and high-frequency noise, respectively. Atomically resolved images, also with a low-pass filter applied, are displayed as insets exhibiting the hexagonal and triangular symmetry as expected for monolayer and multilayer graphene. Triangular symmetries, however, are partly observed on the monolayer, while hexagonal rings are seen on the multilayer, too, as shown in Fig. 11. This renders an assignment just by the appearance of the atomic lattice ambiguous,^{64,66} and calls for the additional characterization by Raman spectroscopy as shown in Fig. 1. The height profiles shown in Fig. 10(c) reveal that the corrugation on the monolayer is significantly larger than on the multilayer. The rms roughness σ can be deduced

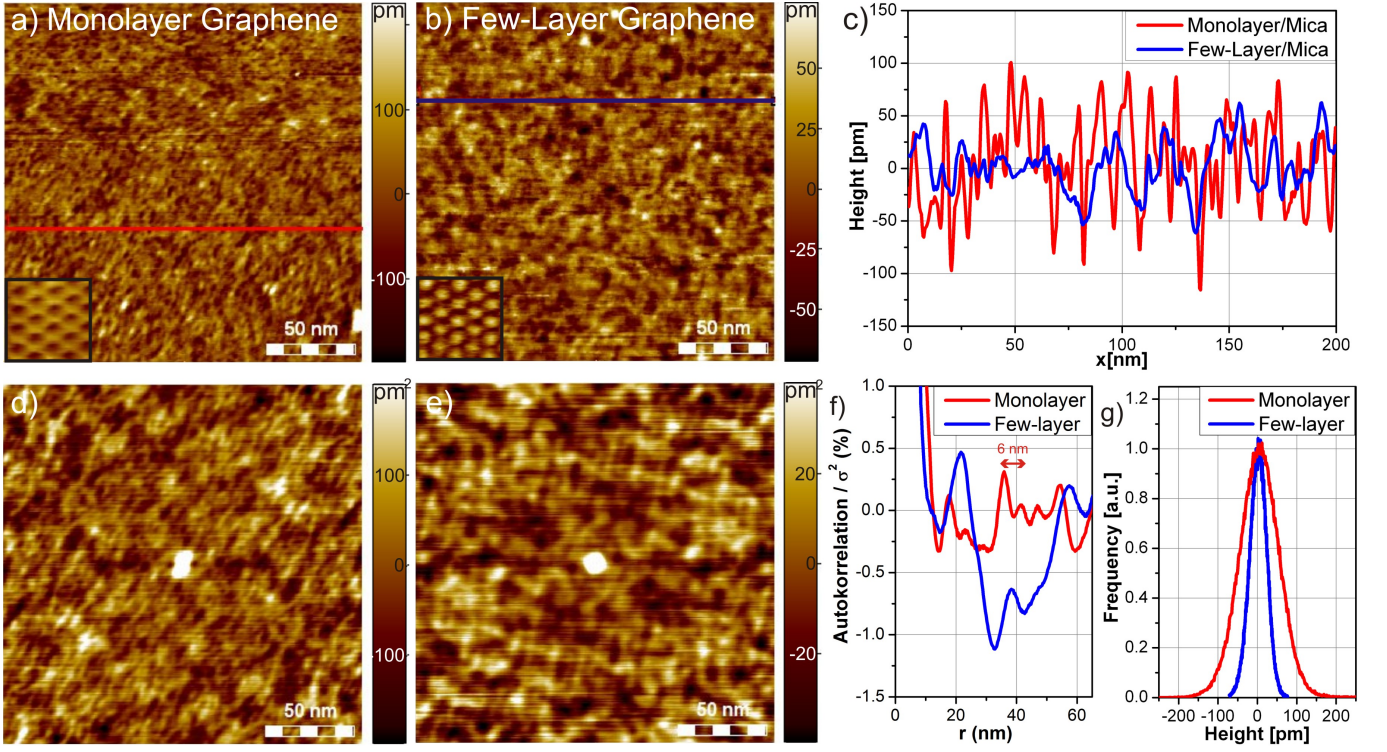


FIG. 10. (a) STM image of monolayer graphene on mica; $V = 0.4$ V, $I = 0.2$ nA, $\sigma = 53.6$ pm; (b) STM image of few-layer graphene on mica; $V = 0.3$ V, $I = 0.15$ nA, $\sigma = 22.2$ pm; insets in (a) and (b): atomically resolved images; (a) $V = -0.4$ V, $I = 0.3$ nA, (b) $V = 0.4$ V, $I = 0.1$ nA; (c) height profiles along the lines marked in (a) and (b) in corresponding color; (d), (e) autocorrelation images $AC(x, y)$ of (a), (b), respectively without any filtering beyond a line fit; (f) radial averages of (d) (red line) and (e) (blue line) with preferential wavelength marked; (g) histograms of the height values found in (a) (red line) and (b) (blue line) normalized to the average height.

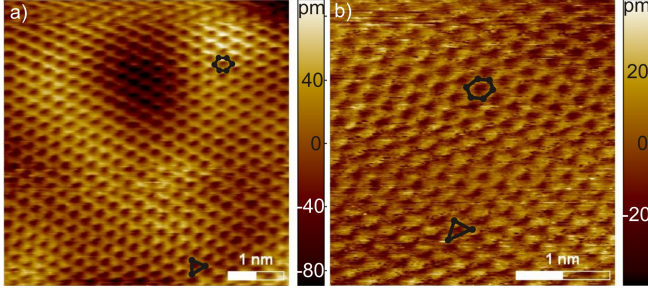


FIG. 11. Atomically resolved STM images on the monolayer (a) and the multilayer (b); different symmetries are indicated as black hexagons and triangles in both images. Images were recorded at (a) $V = -0.4$ V, $I = 0.3$ nA; (b) $V = 0.4$ V, $I = 0.1$ nA.

from the corresponding histograms shown in Fig. 10(g). For few-layer graphene, we find $\sigma = 24 \pm 2$ pm by averaging several images, which is identical to the value found on monolayer graphene by AFM without any heating (24 pm).^{29,67} The monolayer graphene in our STM measurements, however, exhibits a larger roughness of $\sigma = (61 \pm 13)$ pm, where the error bar indicates fluctuations between different measurements. The larger roughness could be due to the fact that our samples, unlike

the samples of Lui et. al.,²⁹ were heated to 180-190°C during contacting which can lead to additional corrugations induced by the different thermal expansion of graphene and substrate.³⁹ The thermal expansion coefficient (TEC) of mica is $7.47 \cdot 10^{-6}$ /K,⁶⁸ while the TEC of monolayer graphene deduced from Raman spectroscopy is about $-4 \cdot 10^{-6}$ /K between 0-200°C.⁶⁹ The latter value is negative and larger than the TEC of graphite, which is $-1.4 \cdot 10^{-6}$ /K at 0°C and $-0.8 \cdot 10^{-6}$ /K at 200°C.⁷⁰ The heating, thus, leads to a tensile strain of $\epsilon = 0.2$ % in the monolayer and $\epsilon = 0.16$ % in the multilayer of graphene at $T = 180^\circ$ C, if we assume a relaxed graphene layer after transfer at 300 K. If the strain is relaxed at the high temperature, a compressive strain with the same absolute value of ϵ builds up during cooling, which might induce additional corrugation. Using a triangular approximation of the rippling with periodicity λ and corrugation height h , one gets:

$$1 + \epsilon = \frac{\sqrt{h^2 + \lambda^2/4}}{\lambda/2} \Rightarrow h \simeq \sqrt{\epsilon/2} \cdot \lambda \quad (4)$$

Deducing from Fig. 10(c) that the dominating periodicity is $\lambda \simeq 8$ nm, we find $h \simeq 250$ pm in good correspondence with the height of the corrugations on the monolayer visible, e.g., in Fig. 10(c). Thus, most likely

TABLE I. Comparison of rms roughness σ for mono- and few-layer graphene λ on mica and SiO₂

System	roughness rms / pm
monolayer / mica	61 ± 13 (this work) 24 ²⁹
few-layer / mica	23 ± 2 (this work)
monolayer / SiO ₂	140-320 ^{39,57,58}

the additional corrugation is induced by heating during the preparation process. It is of course possible that the lateral resolution of 7nm in the AFM measurements of Lui et. al.,²⁹ slightly decreased the observed corrugation with respect to the real one. However, we simulated the topography of the image shown in Fig. 10 (a) as if imaged with a spherical tip always touching the surface but not deforming it and resulting in the apparent width of a step edge given in Ref.²⁹. However, the roughness remains the same (53 nm). This verifies that the roughness is indeed larger by a factor of three after our sample preparation.

The observed change in corrugation height between monolayer and multilayer by a factor of three is similarly observed for graphene on SiO₂, albeit with larger σ values as given in table I.⁵⁷ This relation is probably caused by the larger stiffness of the multilayer. Finally, Fig. 10(d) and (e) show the autocorrelation images $AC(x, y)$ of Fig. 10(a) and (b) calculated as:

$$AC(x, y) = \frac{\sum_{k=0}^{M-1-x} \sum_{l=0}^{N-1-y} z(k, l) \times z(k+x, l+y)}{(M-1-x) \cdot (N-1-y)}, \quad (5)$$

where k and l label the x - and y -positions of individual pixels up to the size of the STM image M, N and $z(k, l)$ is the measured topographic height at the position (k, l) . Prior to determining $AC(x, y)$, we applied a line fit to the STM data in order to remove the influence of occasional changes of the tip, but we checked carefully that this line fit did not induce any novel anisotropy into the $AC(x, y)$ images. No further correction or filtering was applied to the raw STM data used to determine $AC(x, y)$.

Figure 10(d) and (e) show $AC(x, y)$ for monolayer and multilayer, respectively. The $AC(x, y)$ images are cut down to the central $(200 \times 200) \text{ nm}^2$, since they become less meaningful at larger (x, y) as the number of pixels contributing to Eq. 5 is reduced. Both AC -images exhibit a complex pattern with certain regularities. The smallest regular scale can be determined by radial averaging the $AC(x, y)$ data leading to the curves $AC(r)$ with $r = \sqrt{x^2 + y^2}$ as shown in Fig. 10(f). The most obvious oscillation occurs with a wavelength of 6 nm on the monolayer. This number slightly varies for different ar-

eas (10 images evaluated) between 6 nm and 10 nm. Such a preferential wavelength corresponds to the preferential distance between two hills or valleys of the corrugation. The amplitude of this oscillation is only 0.3 % of the value $AC(0 \text{ nm}, 0 \text{ nm}) = \sigma^2$, which would imply that this preferential wavelength contributes only with a tiny fraction (5-6 %) to the total corrugation. A more detailed analysis showed that phase differences of the oscillation in different directions considerably reduce the amplitude in $AC(r)$, i.e. individual profile lines of Fig. 10(d) revealed about the same oscillation period with a larger amplitude of 3-5 % implying that, at least, 15-20 % of the corrugation happens at this wave length. Indeed, the red line section of the STM image of the monolayer in Fig. 10(c) exhibits a preferential distance between peaks of 6-8 nm directly. Of course, we checked that the preferential wave length is not induced by a noise frequency of the instrument and that such a wavelength is not found after using our programme to determine $AC(r)$ for an image with random values on a grid of the same number of pixels. Thus, we have to conclude that preferential wavelengths develop during preparation similar as already observed for graphene on SiO₂.⁵⁷

IV. CONCLUSION

STM measurements on monolayer and multilayer graphene on muscovite mica are presented. On the monolayer, we observe a short-scale corrugation with a preferential wave length of $8 \pm 2 \text{ nm}$ and an rms roughness of $63 \pm 13 \text{ pm}$, the latter being larger than determined previously by AFM.²⁹ The roughness is reduced on few-layer graphene by about a factor of three. On a particular area of the multilayer, a regular pattern of triangles is attributed to a network of partial dislocations separating areas of ABA and ABC stacking. STS measurements revealed that the STM contrast between these areas, exhibiting a size of about $(200 \text{ nm})^2$, is of electronic origin largely dominated by a peak in the local density of states around 0.25 eV above the Dirac point. This peak is only found on ABA areas and might be related to a confinement effect resulting from the topological character of ABC graphene.

ACKNOWLEDGMENTS

We gratefully acknowledge helpful discussions with and hints by E. Obraztsova and financial support by the DFG project Mo858/11-1.

* hattendorf@physik.rwth-aachen.de

¹ K. S. Novoselov, A. K. Geim, S. V. Morozov, D. Jiang, Y. Zhang, S. V. Dubonos, I. V. Grigorieva, and A. A.

- Firsov, *Science* **306**, 666 (2004).
- ² A. H. Castro Neto, F. Guinea, N. M. R. Peres, K. S. Novoselov, and A. K. Geim, *Rev. Mod. Phys.* **81**, 109 (2009).
 - ³ A. K. Geim and K. S. Novoselov, *Nature Mat.* **6**, 183 (2007).
 - ⁴ M. F. Craciun, S. Russo, M. Yamamoto, J. B. Oostinga, A. F. Morpurgo, and S. Tarucha, *Nature Nanotechnol.* **4**, 383 (2009).
 - ⁵ W. Bao, L. Jing, J. Velasco, Y. Lee, G. Liu, D. Tran, B. Standley, M. Aykol, S. B. Cronin, D. Smirnov, M. Koshino, E. McCann, M. Bockrath, and C. N. Lau, *Nature Phys.* **7**, 948 (2011).
 - ⁶ L. Zhang, Y. Zhang, J. Camacho, M. Khodas, and I. Zaliznyak, *Nature Phys.* **7**, 953 (2011).
 - ⁷ C. H. Lui, Z. Li, K. F. Mak, E. Cappelluti, and T. F. Heinz, *Nature Phys.* **7**, 944 (2011).
 - ⁸ F. Guinea, A. H. Castro Neto, and N. M. R. Peres, *Phys. Rev. B* **73**, 245426 (2006).
 - ⁹ S. Latil and L. Henrard, *Phys. Rev. Lett.* **97**, 036803 (2006).
 - ¹⁰ C. L. Lu, C. P. Chang, Y. C. Huang, J. M. Lu, C. C. Hwang, and M. F. Lin, *J. Phys.: Cond. Mat.* **18**, 5849 (2006).
 - ¹¹ C. L. Lu, C. P. Chang, Y. C. Huang, J. H. Ho, C. C. Hwang, and M. F. Lin, *J. Phys. Soc. Jpn.* **76**, 024701 (2007).
 - ¹² M. Aoki and H. Amawashi, *Sol. St. Com.* **142**, 123 (2007).
 - ¹³ S. B. Kumar and J. Guo, *Appl. Phys. Lett.* **98**, 263105 (2011).
 - ¹⁴ A. A. Avetisyan, B. Partoens, and F. M. Peeters, *Phys. Rev. B* **81**, 115432 (2010).
 - ¹⁵ K. Tang, R. Qin, J. Zhou, H. Qu, J. Zheng, R. Fei, H. Li, Q. Zheng, Z. Gao, and J. Lu, *J. Phys. Chem. C* **115**, 9458 (2011).
 - ¹⁶ R. Xiao, F. Tasnádi, K. Koepernik, J. W. F. Venderbos, M. Richter, and M. Taut, *Phys. Rev. B* **84**, 165404 (2011).
 - ¹⁷ N. B. Kopnin, T. T. Heikkilä, and G. E. Volovik, *Phys. Rev. B* **83**, 220503 (2011).
 - ¹⁸ K. F. Mak, J. Shan, and T. F. Heinz, *Phys. Rev. Lett.* **104**, 176404 (2010).
 - ¹⁹ C. H. Lui, Z. Li, Z. Chen, P. V. Klimov, L. E. Brus, and T. F. Heinz, *Nano Lett.* **11**, 164 (2011).
 - ²⁰ S. H. Jhang, M. F. Craciun, S. Schmidmeier, S. Tokumitsu, S. Russo, M. Yamamoto, Y. Skourski, J. Wosnitza, S. Tarucha, J. Eroms, and C. Strunk, *Phys. Rev. B* **84**, 161408 (2011).
 - ²¹ A. Kumar, W. Escoffier, J. M. Poumirol, C. Faugeras, D. P. Arovas, M. M. Fogler, F. Guinea, S. Roche, M. Goiran, and B. Raquet, *Phys. Rev. Lett.* **107**, 126806 (2011).
 - ²² T. Taychatanapat, K. Watanabe, T. Taniguchi, and P. Jarillo-Herrero, *Nature Phys.* **7**, 621 (2011).
 - ²³ T. Khodkov, F. Withers, D. C. Hudson, M. F. Craciun, and S. Russo, *Appl. Phys. Lett.* **100**, 013114 (2012).
 - ²⁴ S. R. Snyder, T. Foeckel, H. S. White, and W. W. Gerberich, *J. Mat. Res.* **7**, 341 (1992).
 - ²⁵ S. R. Snyder, W. W. Gerberich, and H. S. White, *Phys. Rev. B* **47**, 10823 (1993).
 - ²⁶ P. J. Ouseph, *Phys. Rev. B* **53**, 9610 (1996).
 - ²⁷ Y. Kobayashi, K. Takai, K.-i. Fukui, T. Enoki, K. Horigaya, Y. Kaburagi, and Y. Hishiyama, *J. Phys. Chem. Sol.* **65**, 199 (2004).
 - ²⁸ Y. Kobayashi, K. Takai, K.-i. Fukui, T. Enoki, K. Horigaya, Y. Kaburagi, and Y. Hishiyama, *Phys. Rev. B* **69**, 035418 (2004).
 - ²⁹ C. H. Lui, L. Liu, K. F. Mak, G. W. Flynn, and T. F. Heinz, *Nature* **462**, 339 (2009).
 - ³⁰ J. Shim, C. H. Lui, T. Y. Ko, Y.-J. Yu, P. Kim, T. F. Heinz, and S. Ryu, *Nano Lett.* **12**(2), 648 (2012).
 - ³¹ K. Xu, P. Cao, and J. R. Heath, *Science* **329**, 1188 (2010).
 - ³² A. N. Rudenko, F. J. Keil, M. I. Katsnelson, and A. I. Lichtenstein, *Phys. Rev. B* **83**, 045409 (2011).
 - ³³ F. Ostendorf, C. Schmitz, and S. Hirth, *Nanotechnology* **19**, 305705 (2008).
 - ³⁴ F. Ostendorf, C. Schmitz, S. Hirth, A. Kühnle, J. J. Kolodziej, and M. Reichling, *Langmuir* **25**, 10764 (2009).
 - ³⁵ M. Dorn, P. Lange, A. Chekushin, N. Severin, and J. P. Rabe, *J. Appl. Phys.* **108**, 106101 (2010).
 - ³⁶ L. Malard, M. Pimenta, G. Dresselhaus, and M. Dresselhaus, *Phys. Rep.* **473**, 51 (2009).
 - ³⁷ V. Geringer, D. Subramaniam, A. K. Michel, B. Szafraniek, D. Schall, A. Georgi, T. Mashoff, D. Neumaier, M. Liebmann, and M. Morgenstern, *Appl. Phys. Lett.* **96**, 082114 (2010).
 - ³⁸ C. O. Girit and A. Zettl, *Appl. Phys. Lett.* **91**, 193512 (2007).
 - ³⁹ S. Ryu, L. Liu, S. Berciaud, Y.-J. Yu, H. Liu, P. Kim, G. W. Flynn, and L. E. Brus, *Nano Lett.* **10**, 4944 (2010).
 - ⁴⁰ A.-S. Lucier, H. Mortensen, Y. Sun, and P. Grütter, *Phys. Rev. B* **72**, 235420 (2005).
 - ⁴¹ K. T. He, J. D. Wood, G. P. Doidge, E. Pop, and J. W. Lyding, *Nano Lett.* **12**, 2665 (2012).
 - ⁴² J. Hu, X. D. Xiao, D. F. Ogletree, and M. Salmeron, *Nature* **268**, 267 (1995).
 - ⁴³ H. Lipson and A. R. Stokes, *Proceedings of the Royal Society of London. Series A. Mathematical and Physical Sciences* **181**, 101 (1942).
 - ⁴⁴ G. K. Williamson, *Proceedings of the Royal Society of London. Series A. Mathematical and Physical Sciences* **257**, 457 (1960).
 - ⁴⁵ S. Amelinckx and P. Delavignette, *J. Appl. Phys.* **31**, 2126 (1960).
 - ⁴⁶ P. Delavignette and S. Amelinckx, *J. Appl. Phys.* **31**, 1691 (1960).
 - ⁴⁷ P. Delavignette and S. Amelinckx, *J. Nucl. Mat.* **5**, 17 (1962).
 - ⁴⁸ D. J. Bacon, O. Y.N., and D. Rodney, *Dislocations in Solids*, edited by J. Hirth and L. Kubin, Bd. 15 (Elsevier Science, 2009) pp. 21–35.
 - ⁴⁹ M. Morgenstern, D. Haude, V. Gudmundsson, C. Wittneven, R. Dombrowski, C. Steinebach, and R. Wiesendanger, *J. Electr. Spectr. Rel. Phen.* **109**, 127 (2000).
 - ⁵⁰ J. Tersoff and D. R. Hamann, *Phys. Rev. B* **31**, 805 (1985).
 - ⁵¹ J. C. Meyer, A. K. Geim, M. I. Katsnelson, K. S. Novoselov, T. J. Booth, and S. Roth, *Nature* **446**, 60 (2007).
 - ⁵² A. Fasolino, J. H. Los, and M. I. Katsnelson, *Nature Mat.* **6**, 858 (2007).
 - ⁵³ N. D. Mermin, *Phys. Rev.* **176**, 250 (1968).
 - ⁵⁴ W. Bao, F. Miao, Z. Chen, H. Zhang, W. Jang, C. Dames, and C. N. Lau, *Nature Nanotechnol.* **4**, 562 (2009).
 - ⁵⁵ E. Stolyarova, K. T. Rim, S. Ryu, J. Maultzsch, P. Kim, L. E. Brus, T. F. Heinz, M. S. Hybertsen, and G. W. Flynn, *Proc. Natl. Ac. Sci.* **104**, 9209 (2007).
 - ⁵⁶ M. Ishigami, J. H. Chen, W. G. Cullen, M. S. Fuhrer, and E. D. Williams, *Nano Lett.* **7**, 1643 (2007).
 - ⁵⁷ V. Geringer, M. Liebmann, T. Echtermeyer, S. Runte, M. Schmidt, R. Rückamp, M. C. Lemme, and M. Mor-

- genstern, Phys. Rev. Lett. **102**, 076102 (2009).
- ⁵⁸ Y. Zhang, V. W. Brar, F. Wang, C. Girit, Y. Yayon, M. Panlasigui, A. Zettl, and M. F. Crommie, Nature Phys. **4**, 627 (2008).
- ⁵⁹ W. G. Cullen, M. Yamamoto, K. M. Burson, J. H. Chen, C. Jang, L. Li, M. S. Fuhrer, and E. D. Williams, Phys. Rev. Lett. **105**, 215504 (2010).
- ⁶⁰ R. Decker, Y. Wang, V. W. Brar, W. Regan, H.-Z. Tsai, Q. Wu, W. Gannett, A. Zettl, and M. F. Crommie, Nano Lett. **11**, 2291 (2011).
- ⁶¹ H. I. Rasool, E. B. Song, M. J. Allen, J. K. Wassei, R. B. Kaner, K. L. Wang, B. H. Weiller, and J. K. Gimzewski, Nano Lett. **11**, 251 (2010).
- ⁶² N.-C. Yeh, M.-L. Teague, S. Yeom, B. Standley, R.-P. Wu, D. Boyd, and M. Bockrath, Surf. Sci. **605**, 1649 (2011).
- ⁶³ Y. Zhang, T. Gao, Y. Gao, S. Xie, Q. Ji, K. Yan, H. Peng, and Z. Liu, ACS Nano **5**, 4014 (2011).
- ⁶⁴ T. Mashoff, M. Pratzner, V. Geringer, T. J. Echtermeyer, M. C. Lemme, M. Liebmann, and M. Morgenstern, Nano Lett. **10**, 461 (2010).
- ⁶⁵ J. Xue, J. Sanchez-Yamagishi, D. Bulmash, P. Jacquod, A. Deshpande, K. Watanabe, T. Taniguchi, P. Jarillo-Herrero, and B. J. Leroy, Nature Mat. **10**, 282 (2011).
- ⁶⁶ J. Paredes, A. Martinez-Alonso, and J. Tascan, Carbon **39**, 476 (2001).
- ⁶⁷ K. Xu, P. Cao, and J. R. Heath, Science **329**, 1188 (2010).
- ⁶⁸ D. Taylor, Brit. Ceram. Trans. J **87**, 88 (1988).
- ⁶⁹ D. Yoon, Y.-W. Son, and H. Cheong, Nano Lett. **11**, 3227 (2011).
- ⁷⁰ E. Kellett and B. Richards, J. Nucl. Mat. **12**, 184 (1964).